Article

Investigation of Thermal and Spectroscopic Properties of Tellurite-Based Glasses Doped with Rare-Earth Oxides for Infrared Solid-State Lasers

Ahlem Boussetta [1], Aref M. Al-Syadi [2,3], Kamel Damak [4], Ali Erçin Ersundu [5], Miray Çelikbilek Ersundu [5], Essam Ramadan [6], Ali M. Alshehri [7], Khalid I. Hussein [8,*], Ramzi Maalej [4] and El Sayed Yousef [7]

[1] Laboratory of Systems Integration and Emerging Energies, National Engineering School of Sfax (ENIS), University of Sfax, Sfax 3018, Tunisia; ahlem.bousseta@ipeis.usf.tn
[2] Department of Physics, Faculty of Science and Arts, Najran University, Najran 11001, Saudi Arabia; arefalsyadi@yahoo.com
[3] Promising Centre for Sensors and Electronic Devices (PCSED), Advanced Materials and Nano-Research Najran University, Najran 11001, Saudi Arabia
[4] LaMaCoP, Faculty of Sciences of Sfax, University of Sfax, Sfax 3018, Tunisia; kamel.damak@ipeis.usf.tn (K.D.); ramzi.maalej@fss.usf.tn (R.M.)
[5] Department of Metallurgical and Materials Engineering, Yildiz Technical University, Davutpasa Campus KMA-205, Esenler, Istanbul 34220, Turkey; ersundu@yildiz.edu.tr (A.E.E.); miray@yildiz.edu.tr (M.Ç.E.)
[6] Physics Department, Faculty of Science, Al Azhar University, Assuit Assiut 71542, Egypt; esam_ramadan2008@yahoo.com
[7] Department of Physics, Faculty of Science, King Khalid University, Abha P.O. Box 9004, Saudi Arabia; amshehri@kku.edu.sa (A.M.A.); ayousf@kku.edu.sa (E.S.Y.)
[8] Department of Radiological Sciences, College of Applied Medical Sciences, King Khalid University, Abha 61421, Saudi Arabia
* Correspondence: kirahim@kku.edu.sa

Abstract: The thermal and optical properties of 60TeO$_2$-20K$_2$TeO$_3$-10WO$_3$-10Nb$_2$O$_5$ (in mol%) glasses doped with Ho$_2$O$_3$, Er$_2$O$_3$, and Tm$_2$O$_3$ were explored in the present work. The thermal stability, refractive index n, extinction coefficient k, absorption coefficient α, and optical band gap of the glasses were evaluated. The UV–Vis–NIR absorption spectra, the Judd–Ofelt intensity parameter, the spectroscopic quality factor, and the emission and absorption cross-sections were calculated to investigate the effects of Er^{3+} and Tm^{3+}, respectively, on the band spectroscopic properties of Ho^{3+} ions. The results showed that the maximum emission cross-section was approximately 8×10^{-21} cm^2, and the values of the full width at half maximum (*FWHM*), quality factor ($\sigma_e \times FWHM$), and gain coefficient of Ho^{3+}: $^5I_7 \rightarrow {}^5I_8$ were also reported. The value of the *FWHM* $\times \sigma_e$ was 1200×10^{-28} cm^3, which showed greater gain characteristics than earlier study results. For 2 µm mid-infrared solid-state lasers, the glasses that were examined might be a good host material.

Keywords: co-doped tellurite glasses; rare earth; DSC; thermal properties; refractive index; Judd–Ofelt analysis; gain quality

1. Introduction

Lasers, optical fiber amplifiers, flat-panel displays, optoelectronics, memory devices, solar cells, and light-emitting diodes are just a few of the numerous technical and scientific uses of glasses [1,2]. Oxide glasses often have several desirable characteristics, including low optical properties thresholds, and great transparency. Several researchers have been actively working to change these materials to acquire significant nonlinear coefficients, which are needed for using them in nonlinear optical devices [1–3]. It is well known that tellurite-based glasses are transparent in the mid-infrared range, have a high refractive index, and a high density. Not only are these glasses non-toxic, but they also resist moisture and are stable against devitrification. These characteristics make the glasses useful in

many fields, including laser windows, nonlinear optical devices (including limiters, optical switches, and modulators), and optical fibers [4]. The addition of rare-earth ions is essential for white-light-emitting diodes, and glass systems based on TeO_2 are very promising matrices for this purpose [5]. There has been a recent renaissance in the study of earth-doped materials for photonic applications, display monitors, X-ray imaging, scintillators, lasers, up-conversion, and amplifiers for fiber-optic communications [5–7]. Rare-earth-doped glasses have important applications in solid laser sources, optical sensors, solar cells, optical telecommunication, white-light-emitting diodes, and optical data storage devices [7,8]. Tellurite glasses with added transition metal oxides should have a higher softening point and more stability, as seen with WO_3 [9]. The WO_3 and TeO_2 components of the glass are network formers. WO_4 tetrahedral and WO_6 octahedral structural units and TeO_3 trigonal pyramid and TeO_4 trigonal bipyramid units are the two different kinds of dopant sites that are present in the glass because of this [10]. The two different types of dopant sites vary in the intensity of their ligand fields and, as a result, in their distributions in space due to their unique geometries [5]. According to Pandey et al. [6], the third nonlinearity effect is due to the ability of WO_3 to increase the density of the non-bridging oxygen atoms, which causes the optical band gap to increase in Bi_2O_3-WO_3-TeO_2 glasses. According to Kim and Yoko [11], the optical band gap, third-order susceptibility, $\chi^{(3)}$, real refractive index, static refractive index, and empty d-shell transition metal cations, including Nb^{5+} cations, affect oxide glasses.

The present work aims to study the optical properties of the TeO_2-K_2TeO_3-WO_3-Nb_2O_5 glass system, doped with rare-earth oxides (Ho_2O_3, Er_2O_3, and Tm_2O_3). The optical characteristics are correlated with the structure's phase transitions and thermal stability, which are determined using differential scanning calorimetry and a double-beam spectrophotometer. The ultraviolet–visible–near-infrared (UV–Vis–NIR) absorption and emission spectra of Ho^{3+}-single-doped, Ho^{3+}/Er^{3+}-co-doped, and Ho^{3+}/Tm^{3+}-co-doped tellurite glasses (TKWN1, TKWN2, and TKWN3, respectively) were analyzed at room temperature. Based on the Judd–Ofelt theory, the detailed spectroscopic parameters, radiative transition probabilities, radiative lifetimes, and branching ratios of the TKWN1 sample were obtained. Moreover, the absorption and emission cross-sections of Ho^{3+} were calculated via McCumber theory. In addition, the gain coefficient of Ho^{3+}: $^5I_7 \rightarrow {}^5I_8$, the quality factor $\left(\sigma_e^{peak} \times FWHM\right)$, and the full width at half maximum ($FWHM$) were also reported. Finally, the possible visible and NIR emissions and their applications for future green laser sources and optical amplifiers were discussed.

2. Experimental Section

Using the melt quench technique, tellurite-based glasses with the composition ($60TeO_2$-$20K_2TeO_3$-$10WO_3$-$10Nb_2O_5$) mol%, doped with rare-earth oxides (Ho_2O_3, Er_2O_3, and Tm_2O_3 in ppm ratio), were prepared. The details of their composition are shown in Table 1. The powder was mixed and heated in a platinum crucible in a furnace at 960 °C for 35 min. Subsequently, the highly viscous melt was cast into a graphite mold. The quenched glass was annealed at 250 °C for 2 h and then slowly cooled to room temperature (RT). The color of the prepared samples depended on the ratio of NiO in the glasses (as clarified in Figure 1). The thermal analysis of the glasses was carried out via differential scanning calorimetry (DSC Shimadzu 50) with a heating rate of 10 °C/min in the range of 20–550 °C. The density of the glass samples was evaluated using the Archimedes method.

$$\rho = \frac{W_{air} \times \rho_l}{(W_{air} - W_l)} \tag{1}$$

where W_{air} and W_L are the weights of the glass sample in air and toluene, respectively. ρ_l is the density of toluene liquid ($\rho_l = 0.865$ gm·cm^3).

Table 1. Composition, density ρ, molar volume V_m, and oxygen packing density (OPD) of TKWN glasses.

Sample	Composition (mol%)	ρ (g/cm^3)	V_m (cm^3/mol)	OPD (mol/L)
TKWN1	60TeO$_2$-20K$_2$TeO$_3$-10WO$_3$-10Nb$_2$O$_5$-30,000 ppmHo$_2$O$_3$	4.9125	41.07	65.51
TKWN2	60TeO$_2$-20K$_2$TeO$_3$-10WO$_3$-10Nb$_2$O$_5$-30,000 ppmHo$_2$O$_3$-30,000 ppm Er$_2$O$_3$	4.9597	41.80	66.51
TKWN3	60TeO$_2$-20K$_2$TeO$_3$-10WO$_3$-10Nb$_2$O$_5$-30,000 ppmHo$_2$O$_3$-30,000 ppm Tm$_2$O$_3$	4.9641	41.78	66.53
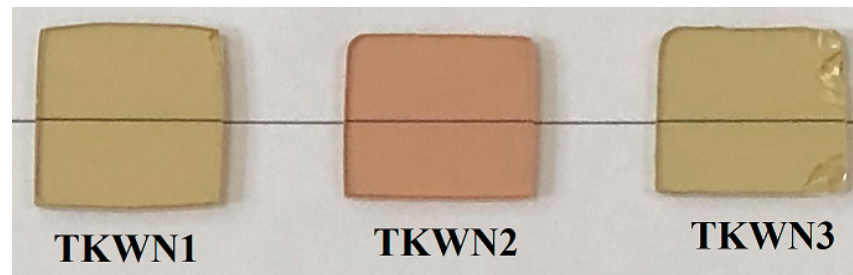
Figure 1. Photographs of as-prepared TKWN glasses.

The optical absorption and transmission spectra were measured in the wavelength range of 400–2500 nm using aJASCO V-570 spectrophotometer (JASCO INTERNATIONAL CO., LTD. Tokyo, Japan).

3. Results and Discussion

3.1. Density, Molar Volume, and Oxygen Packing Density

The density (ρ), molar volume (V_m), and oxygen packing density (OPD) of the studied glasses are listed in Table 1. The density of the glasses varied between 4.9125 and 4.9641 g/cm^3. The addition of rare-earth oxides to TeO$_2$-based glasses leads to a relatively slight increase in density. This increase is related to the molecular weights of rare-earth oxides, which are much greater than those of other constituents in the studied TeO$_2$-based glass, and also to the change in the coordination number of rare-earth ions [12,13]. Therefore, the densities of the glasses co-doped with the two types of rare-earth oxides, Ho$_2$O$_3$ and Er$_2$O$_3$ (TKWN2 sample) and Ho$_2$O$_3$ and Tm$_2$O$_3$ (TKWN3 sample), were relatively higher than the glass doped with Ho$_2$O$_3$ only (TKWN1 sample). Furthermore, the molecular weights of Er$_2$O$_3$ and Tm$_2$O$_3$ (382.5 and 385.866 g/mol, respectively) are higher than that of Ho$_2$O$_3$ (377.858 g/mol), which led to an increase in the density of the TKWN2 and TKWN3 glasses compared to the TKWN1 glass. Given that the density is inversely proportional to the molar volume and proportional to the average molecular weight, it is reasonable to assume that the two quantities will behave in opposition to one another in most amorphous materials (especially glass). In this glass system, the TKWN1 glass, doped only with Ho$_2$O$_3$, exhibited the reverse behavior, with a reduced density and molar volume. Previous reports [13,14] describe this unusual behavior for several glass systems containing rare-earth elements. It is well known that changes in molecular weight and density have an impact on the extent to which the molar volume changes. In comparison to the TKWN2 and TKWN3 glasses, the rate of change in the molar volume of the TKWN1 glass was lower. Hence, the network became more closed and tightly packed. This behavior could have been due to the addition of Er$_2$O$_3$ and Tm$_2$O$_3$ to the TKWN2 and TKWN3 glasses, respectively.

3.2. Thermal Properties

The DSC curves of the TKWN glasses doped with rare-earth oxides and tempered at a rate of 10 °C/min are illustrated in Figure 2. This glassy material's thermal stability was confirmed by the DSC traces that were obtained for the samples. Each DSC scan exhibited a small endothermic peak corresponding to the glass transition temperature

(T_g), followed by exothermic peaks, with two peaks (T_{p1} and T_{p2}) for the TKWN1 sample and one peak (T_{p1}) for the TKWN2 and TKWN3 samples, which corresponded to the crystallization temperature. The glass transition temperature (T_g), onset crystallization temperature (T_c), and peak crystallization temperatures (T_{p1} and T_{p2}) were measured and recorded, as shown in Table 2. The T_g provides information about the strength of the bonds and connectivity in the glass network, i.e., the T_g increases with the increasing connectivity and bond strength in the glass [15]. The values of T_g for the present glass system were close to those of TeO_2-based glasses [16,17], which show high T_g values. The increase in the T_g values can result from the combined effect of incorporating both Nb_2O_5 and WO_3 [18–21]. From Table 2, it is clear that the doping of the TKWN glasses with Er_2O_3 and Tm_2O_3 had a strong influence on the T_g as well as the onset and peak crystallization temperatures (T_c and T_p), which shifted to significantly higher temperatures (as shown in Figure 2).
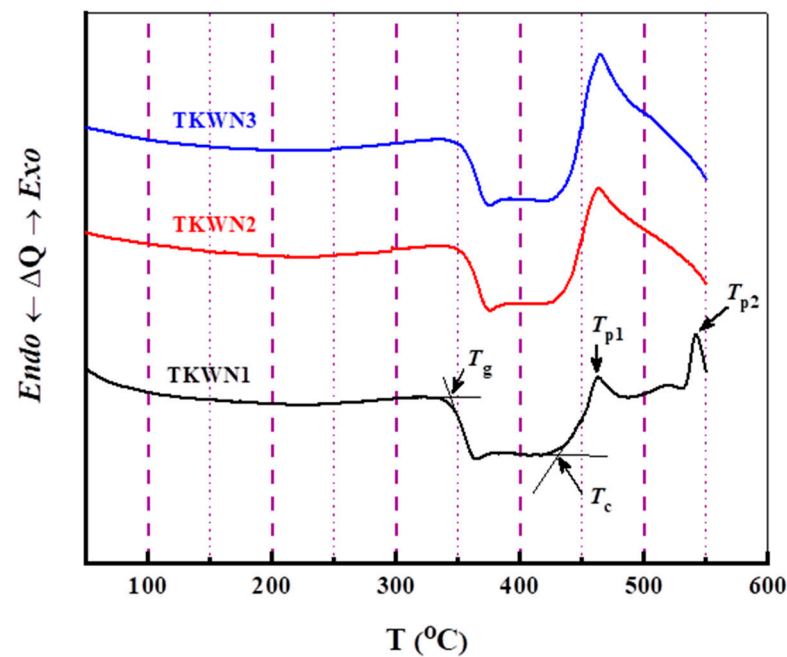

Figure 2. DSC curves of TKWN glasses at heating rate of 10 °C/min.

Table 2. Values of T_g, T_c, T_p, ΔT, H, and *KSP* for TKWN glasses.

Sample Code	T_g °C	T_c °C	T_{p1} °C	T_{p2} °C	ΔT °C	H	K_{SP} °C
TKWN1	344	431	462	542	87	0.253	10.63
TKWN2	355	438	463	-	83	0.234	7.61
TKWN3	356	439	464	-	83	0.233	7.58

We found that adding Er_2O_3 and Tm_2O_3 to the TKWN glass doped with Ho_2O_3 improved the value of T_g. This might have been because the bonds were very strong. Thus, the as-prepared glasses were more rigid and had better glass-forming capabilities after adding rare-earth oxides [14]. A further explanation for the reported increase in the T_g with increasing rare-earth oxide concentrations might be the OPD, as shown in Table 1. The OPD is a measure of the closeness of the oxide network's packing. As the concentration of rare-earth oxides increases, it is evident that the OPD increases as well. This suggests that as the amount of rare-earth oxides grows, the structure becomes more compact. The presence of rare-earth oxides in the glass system suggests the production of a more compact macromolecular chain, which in return increases the T_g, since a closer macromolecular structure requires greater internal energy for chain mobility, which is necessary for the glass transition [22].

An estimate for the thermal stability of glass has been calculated utilizing the thermal stability factor $\Delta T = (T_c - T_g)$. To achieve the required large working range, e.g., during the fabrication process, it is favorable to have ΔT values that are as large as possible [23–26]. Hruby's equation, namely $H = \Delta T/T_g$, and the glass compositional dependencies of Hruby's coefficient were estimated by Sestak [27,28]. Table 2 displays Hruby's coefficient (H) and the thermal stability factor (ΔT); these are important in evaluating the glass devitrification process [29,30]. It was observed that the thermal stability of the studied glasses decreased with increasing rare-earth oxide concentrations. The parameter K_{SP}, which is related to the stability of glass against crystallization, can be calculated using the following relationship [31]:

$$K_{SP} = \frac{(T_p - T_c)(T_p - T_g)}{T_g} \tag{2}$$

where T_g is the glass transition temperature, T_c is the onset crystallization temperature, and T_p is the peak crystallization temperature.

Table 2 shows the KSP values for the as-prepared glasses, which lay within the range of those of tellurite-based glasses, which include alkaline and heavy metal ions, as reported in Refs. [16,31,32].

3.3. Optical Properties

The optical transmission spectra of the TKWN glasses doped with rare-earth oxides are illustrated in Figure 3. From this figure, we can see several peaks in the spectrum, which are due to the presence of rare-earth ions (Ho^{3+}, Er^{3+}, and Tm^{3+}) in the glasses. Figures 4 and 5 show the optical absorption spectra of the as-prepared glasses. Numerous peaks are due to the presence of rare-earth ions in the glass. The absorption coefficient (α) for the as-prepared glasses was calculated using the following equation [33]:

$$\alpha = \frac{1}{d}ln\left(\frac{I_0}{I_t}\right) = 2.303\frac{A}{d} \tag{3}$$

where I_0, I_t, A, and d are the incident intensity, transmitted intensity, absorbance, and thickness of the film, respectively.
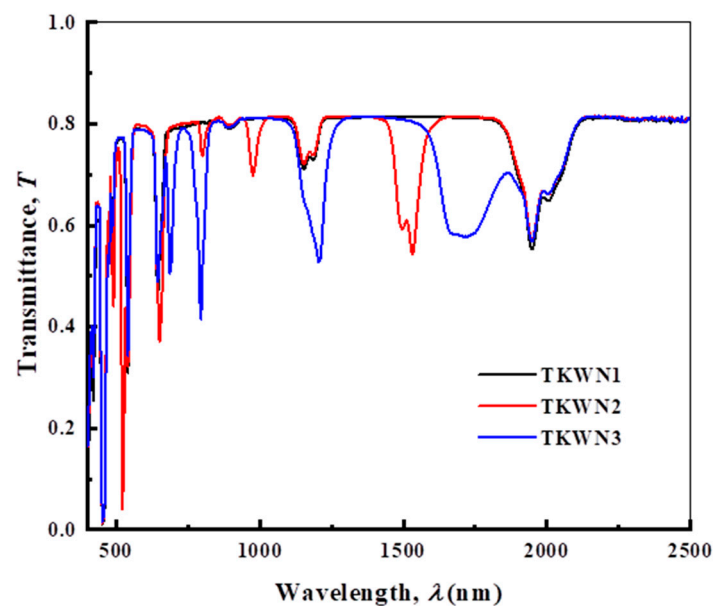

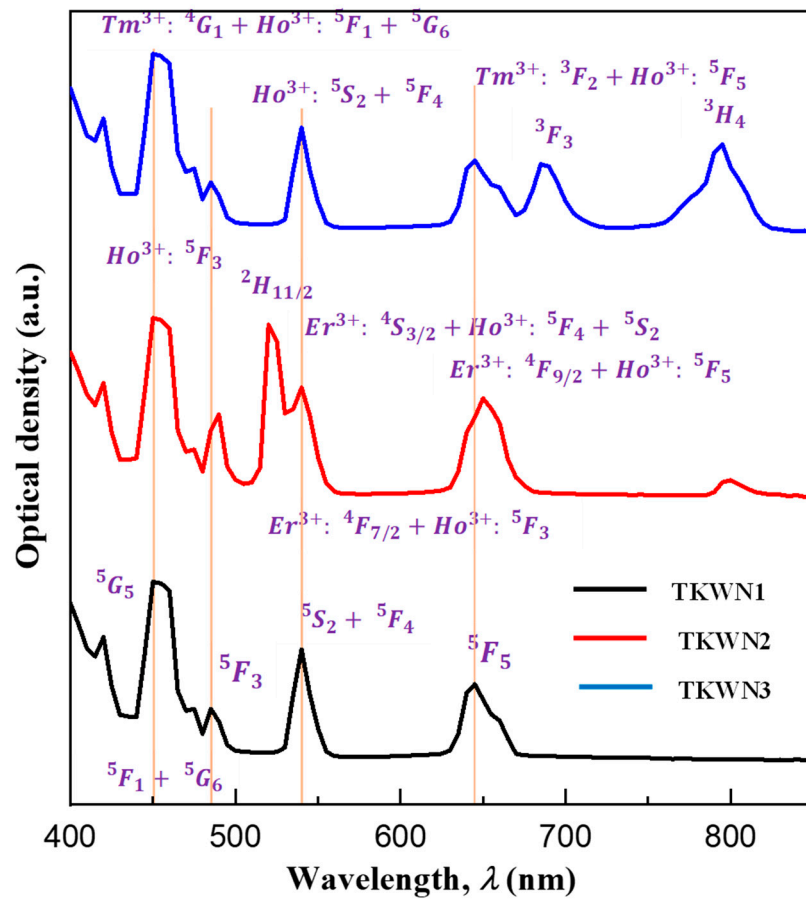**Figure 3.** Optical transmission spectra of TKWN glasses.

Figure 4. Room-temperature optical absorption spectra of TKWN glasses near UV–visible range.
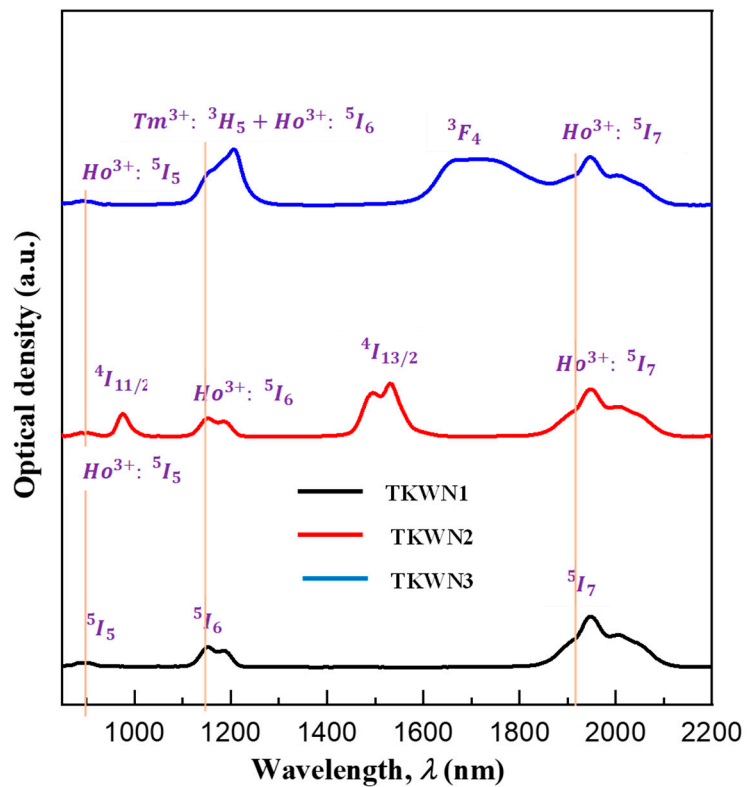

Figure 5. Room-temperature optical absorption spectra of TKWN glasses near infrared range.

When designing devices that include glass, the material's refractive index is an essential parameter that must be considered. The following equation expresses the relationship between the reflectance (R) and extinction coefficient (k) using the value of the real component of the complex refractive index (n), according to Fresnel's theory of light reflectivity:

$$R = \frac{(n-1)^2 + k^2}{(n+1)^2 + k^2} \tag{4}$$

The value of k can be calculated according to the following equation [34]:

$$k = \frac{\alpha\lambda}{4\pi} \tag{5}$$

where λ is the wavelength in micrometers.

The calculated n and k values of the TKWN glasses doped with rare-earth oxides are given in Figures 6 and 7, respectively. As shown in Figure 6, the refractive index (n) decreased when increasing the wavelength of the incident photon.
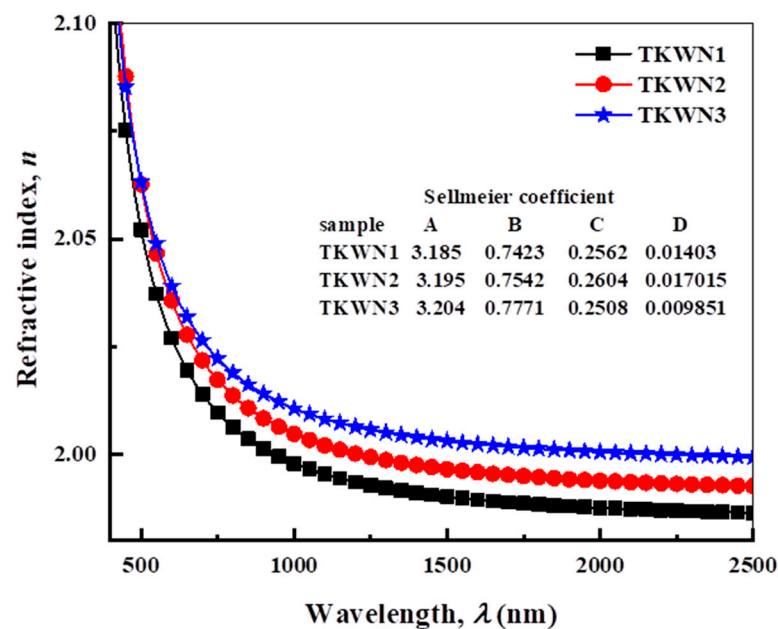

Figure 6. Dependence of refractive index (n) on wavelength (λ) for TKWN glasses.

The density, the electronic polarizability of the oxide ion, the coordination number, and the polarizability of the initial neighbor ions coordinated with it (anions) are among the several important variables that impact the refractive index [21]. The Er_2O_3 or Tm_2O_3 added to the TKWN glass doped with Ho_2O_3 caused a minor increase in the n values. In addition, we found that the density, ρ, and n had a linear relationship. See Figure 6 for the highest values of n for the TKWN glass samples doped with both Ho_2O_3 and Tm_2O_3.

The Sellmeier dispersion formula is one of the most well-known fitted dispersion equations that describes the index variation, n, vs. the wavelength, λ. The five coefficients included in this formula allow it to fit the data perfectly throughout a wide spectrum range, in agreement with the observations. One means to describe the propagation characteristics of waveguides constructed from the materials under study is to employ the dispersion data in the form of fitting Sellmeier coefficients. The following is the Sellmeier dispersion formula in the spectra of the absorption bands; when ($h\nu$) is smaller than (E_{opt}), the photon band gap energy is as follows [35,36]:

$$n^2(\lambda) = A + B / \left(1 - \frac{C}{\lambda^2}\right) + D / \left(1 - \frac{E}{\lambda^2}\right) \tag{6}$$

where λ is the wavelength in micrometers. In this case, the glass materials' dispersion characteristics are *A*, *B*, *C*, *D*, and *E*. The first and second terms relate to the refractive index contributions of larger and lower energy gaps from electronic absorption. The last term indicates how the lattice absorption causes the refractive index to decrease [35,36]. Equation (6) was used to fit the experimental data, yielding the Sellmeier coefficients shown in Table 3. Figure 6 shows the refractive index behavior for the as-prepared glasses with the wavelength calculated using Sellmeier's equations [35].
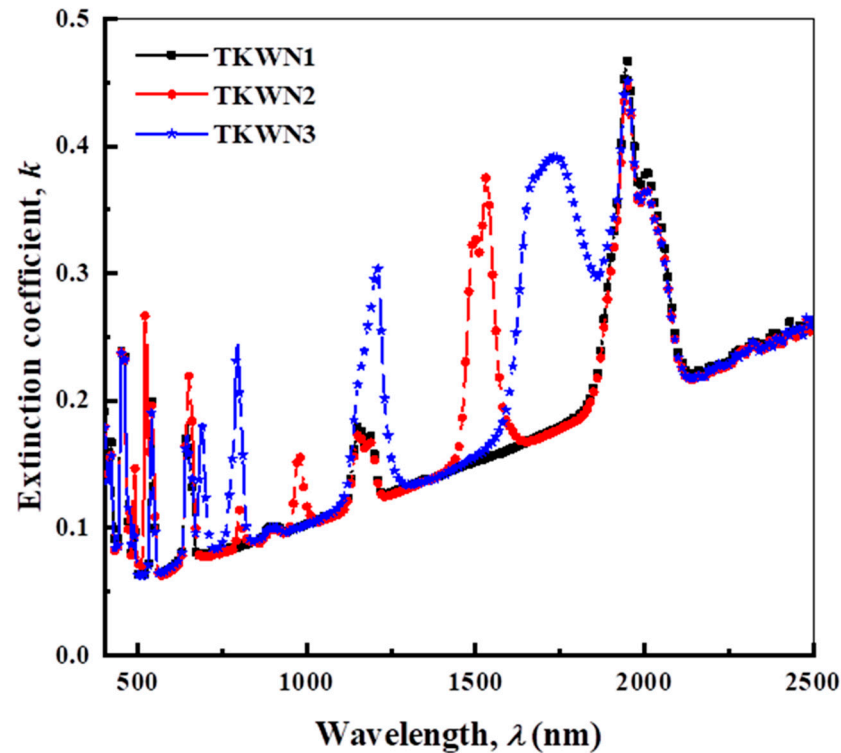

Figure 7. Dependence of extinction coefficient (k) on wavelength (λ) for TKWN glasses.

Table 3. Values of *A*, *B*, *C*, *D*, E_{opt}, R_m, α_m, and *M* for TKWN glasses.

Sample Code	Sellmeier Coefficients				E_{opt} (eV)	R_m Mol^{-1}	α_m Å^{-3}	*M*
	A	*B*	*C*	*D*				
TKWN1	3.185	0.7423	0.2562	0.01403	2.453	20.30	8.05	0.506
TKWN2	3.195	0.7542	0.2604	0.017015	2.481	20.75	8.23	0.504
TKWN3	3.204	0.7771	0.2508	0.009851	2.501	20.84	8.26	0.501

Furthermore, $E_g = 1.24/\lambda$ is the average absorption band gap, E_g (measured in electron volts), and it may be used to determine the lattice absorption frequency or E_g [35]. For more information about optically induced transitions and optical band gaps in materials, it is helpful to investigate their optical absorption edges. The basic idea behind this processing is the absorption of photons whose energies are higher than the energy of the band gap. At the basic absorption edge, electromagnetic waves interact with electrons in the valence band to cause two types of optical transitions: direct and indirect. The Tauc relation [37] provides the relationship between α and the photon energy of the incoming radiation, $h\nu$.

$$\alpha\, h\nu = b\left(h\nu - E_{opt}\right)^s \tag{7}$$

where ν is the frequency and *h* is the Planck constant. While *b* remains constant, the value of *s* varies according to the interband transition process. The parameter *s* takes the value of ½ in the case of the direct allowed transition, while it is equal to 2 in the case of the indirect

allowed transition. Equation (7), which is associated with indirect permitted transitions in most types of glass, shows a straight line for s = 2. The Tauc plot of $(\alpha h\nu)^{1/2}$ against $(h\nu)$ for the as-prepared glasses is shown in Figure 8. To determine the E_{opt} of these glasses, we extrapolated their linear domains at the absorption edge to intersect the $h\nu$ axis at $(\alpha h\nu)^{1/2} = 0$. Table 3 lists the E_{opt} values. Adding Er_2O_3 or Tm_2O_3 to the TKWN glass doped with Ho_2O_3 slightly increased the E_{opt} value; it was greatest in the TKWN glass sample that was co-doped with Ho_2O_3 and Tm_2O_3. As mentioned previously regarding the thermal properties and density of the proposed glass material, the strong bonds are the expected cause of the increase in the E_{opt}. values. The results for the present glass material show that when the amount of rare-earth oxides is increased, the structure becomes more closely packed, leading to an increase in the T_g, ρ, and OPD. Hence, increasing the number of rare-earth oxides in the glass system is suggested to form a more rigid macromolecular chain, which decreases the amount of non-bridging oxygen (NBO) and increases the E_{opt}.
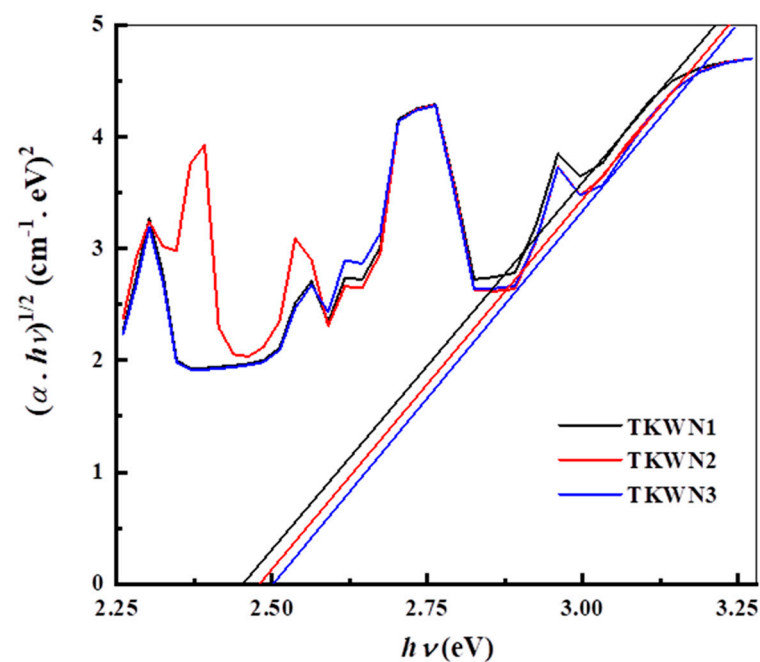

Figure 8. Plot of $(\alpha h\nu)^{1/2}$ against $h\nu$ for TKWN glasses.

By applying the Wemple–DiDomenico (WDD) relationship to the model of a single oscillator, we may describe the dispersion of n [38].

$$n^2 = 1 + \left(\frac{E_d E_o}{E_o^2 - (h\nu)^2} \right) \qquad (8)$$

where E_d is the dispersion energy, which represents the average strength of the interband optical transitions, and E_o is the energy of the effective dispersion oscillator or the average energy gap. Figure 9 shows the variation in $(n^2 - 1)^{-1}$ versus $(h\nu)^2$ for the studied glasses. The values of E_d and E_o can be directly determined from the slope $(E_o E_d)^{-1}$ and the intercept on the vertical axis (E_d / E_o). The static refractive index (n_0) of the as-prepared glasses is calculated via the extrapolation of the Wemple–DiDomenico dispersion relation, Equation (8), when $h\nu \rightarrow 0$, and this gives the following expression:

$$n_0 = \sqrt{1 + E_d / E_o} \qquad (9)$$

where n_o is the static refractive index. The deduced values of E_o, E_d, and n_o are listed in Table 4. It is observed that the value of n_o for the as-prepared glasses increases with

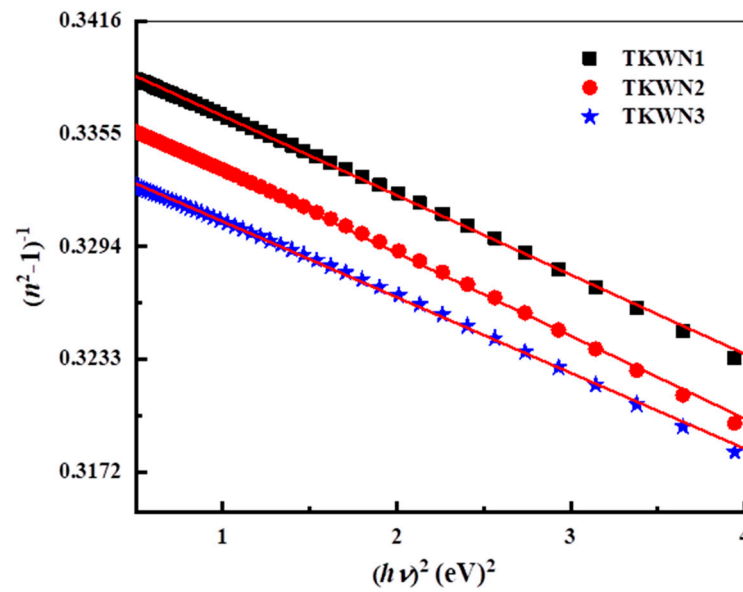an increase in density. Figure 10 shows that n^2 is strongly dependent on λ^2 according to Equation (6).

Figure 9. Plot of $(n^2 - 1)^{-1}$ as a function of $(h\upsilon)^2$ for TKWN glasses.

Table 4. Optical parameters of TKWN glasses.

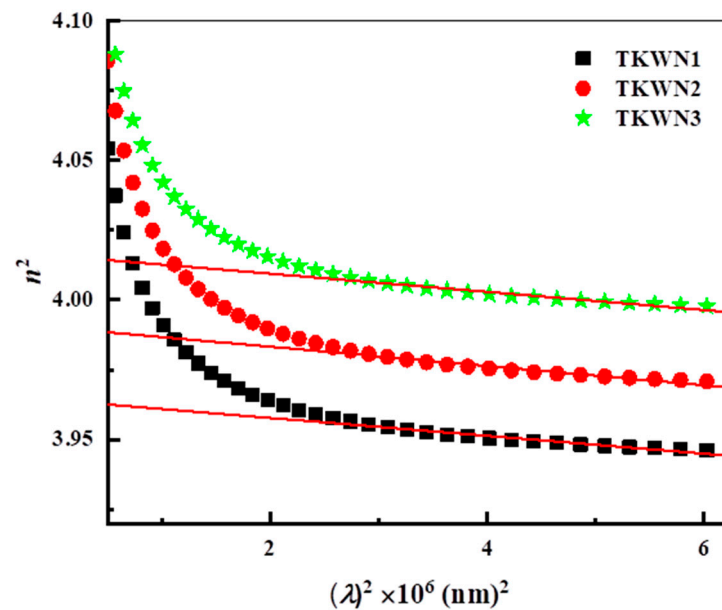| Sample Code	Dispersion Parameters		
	E_o (eV)	E_d (eV)	n_o
TKWN1	8.60	25.25	1.983
TKWN2	8.68	25.69	1.989
TKWN3	9.03	26.98	1.996

Figure 10. Variation in n^2 as a function of λ^2 for TKWN glasses.

A suitable method for the investigation of the impact of ionic packing on the refractive index (n) of glass is to calculate its molar refractivity (R_m), which is defined as the total polarizability of a mole of a material and derived from the following formula [33]:

$$R_m = \left(\frac{n_o^2 - 1}{n_o^2 + 2} \right) V_m \tag{10}$$

where V_m is the molar volume.

According to the following Clasius–Mosotti relationship, the molar electronic polarizability of a material is proportional to its molar refractivity, which, in effect, corresponds to the glass's structure [33].

$$\alpha_m = \left(\frac{3}{4\pi N_A} \right) R_m \tag{11}$$

where N_A is Avogadro's number. The values of R_m and α_m are listed in Table 3. These values increase with the increase in the rare-earth content. The metallization criterion (M) gives information about the metallic or non-metallic nature of the glass, and it is calculated through the following relationship [31]:

$$M = 1 - \frac{R_m}{V_m} \tag{12}$$

If $M > 0$, the materials demonstrate an insulating nature, but if $M < 0$, the materials exhibit a metallic nature. The results of the metallization criterion (M) are listed in Table 3 and are within the range of 0.501–0.506. Therefore, the as-prepared glasses demonstrate an insulating nature [16,31].

3.4. Absorption Spectra, Judd–Ofelt Analysis, and Radiative Properties

Extrinsic absorption, which is associated with internal electronic transitions, particularly in the 4f shells of rare-earth ions, and intrinsic absorption, which occurs at short and long wavelengths, are the two processes that lead to the development of the optical spectra of single-rare-earth-doped or co-doped glasses [39,40].

The room-temperature UV–Vis–NIR absorption spectra recorded in the range of 400–2500 nm for the Ho^{3+}-single-doped, Ho^{3+}/Er^{3+}-co-doped, and Ho^{3+}/Tm^{3+}-co-doped tellurite glasses (TKWN1, TKWN2, and TKWN3, respectively) and the absorption peaks related to electronic transitions from the ground states of Ho^{3+}, Er^{3+}, and Tm^{3+} to their corresponding excited levels are presented in Figures 4 and 5, respectively. The eight absorption peaks from the ground state Ho^{3+} are responsible for the bands at the wavelengths of 420, 450, 485, 540, 645, 890, 1155, and 1950 nm for Ho^{3+}: $^5I_8$ regarding the degree of intensity; correspondingly, the resulting values are $^5G_5$, $^5F_1+^5G_6$, $^5F_3$, $^5S_2+^5F_4$, $^5F_5$, $^5I_5$, $^5I_6$, and $^5I_7$. The seven absorption peaks from the ground state Er^{3+} are Er^{3+}: $^4I_{15/2}$ to the excited levels $^4F_{7/2}$, $^2H_{11/2}$, $^4S_{3/2}$, $^4F_{9/2}$, $^4I_{9/2}$, $^4I_{11/2}$, and $^4I_{13/2}$, respectively. The bands with peaks at the wavelengths of 450, 645, 685, 795, and 1710 nm are derived from the five absorption peaks that start the transition of the ground state Tm^{3+}, namely Tm^{3+}: $^3H_6$ to the excited levels $^1G_4$, $^3F_2$, $^3F_3$, $^3H_3$, $^3H_5$, and $^3F_4$, respectively. These are identical to the absorption peaks seen in other glasses [41–43].

Figure 4 further confirms that the presence of Er^{3+} or Tm^{3+} ions in the matrix causes absorption bands to form due to the energy-level quantum structures in these ions [44]. In photoluminescence measurements, the 808 nm commercial laser diode (LD) can be utilized as a pumping source because although Ho^{3+} ions do not exhibit any clear absorption peaks around 808 nm or 980 nm, the $^3H_4$ ground state of Tm^{3+} and the $^4I_{9/2}$ ground state of Er^{3+} both exhibit an absorption peak at around 800 nm. The locations of the absorption peaks exhibit no apparent variations when compared to the Ho^{3+}-single-doped sample (TKWN1). In addition, the two Ho^{3+}/Er^{3+}-co-doped tellurite glasses (TKWN2 and TKWN3, respectively) match the tellurite glass samples in terms of the forms and peak locations of each transition [45–47]. In order to investigate the potential spectroscopic parameters of

the single-doped sample (TKWN1), the Judd–Ofelt (JO) theory is adopted without taking into account the energy transfer and multiphonon de-excitation probabilities. Detailed applications of the JO model have been described in other papers [48,49]. We compute the experimental electric dipole line strength (S_{ed}^{mes}) of the Ho^{3+}-single-doped glass sample (TKWN1) using the absorbance spectra (Figures 4 and 5). Unlike the glasses doped with other rare-earth ions, such Er^{3+} and Tm^{3+}, the magnetic dipole transitions in the Ho^{3+}-ion-doped glass are sufficient to be undetectable [50]. Thus, the magnetic dipole transitions should be taken into account when we calculate the experimental electric dipole line strength (S_{ed}^{mes}). The calculated values are given in Table 5, along with the values of the magnetic dipole line strength S_{md}, the three phenomenological intensity parameters Ω_t ($t = 2,\ 4,\ 6$), and the calculated electric dipole line strength (S_{ed}^{cal}). As shown in Table 5, good agreement is found between the calculated and the experimental values, and the lower value of the root mean square deviation between the experimental and the calculated line strengths of the transitions $(\delta_{rms} = 0.5659 \times 10^{-20}\ cm^2)$ indicates the validity of JO theory for the prediction of the spectral intensity of Ho^{3+}.

Table 5. Values of average wavelengths, refractive indices, integrated absorption coefficients, and electric and magnetic dipole line strengths for Ho^{3+}-single-doped tellurite glass (TKWN1).

Transition from $^5I_8$ to	$\overline{\lambda}$ *(nm)*	n	$\int OD(\lambda)d\lambda$ (nm)	S_{ed}^{cal} (pm²)	S_{ed}^{mes} (pm²)	S_{md} (pm²)
$^5I_7$	1950	1.9884	25.9613	1.9518	1.2918	0.9493
$^5I_6$	1155	1.9959	5.0289	0.8340	1.0327	0
$^5I_5$	895	2.0041	0.52004	0.1202	0.1370	0
$^5F_5$	645	2.0226	6.0251	1.4788	2.1687	0
$^5S_2+^5F_4$	540	2.0420	4.65323	1.4749	1.9679	0
$^5F_3$	485	2.0609	0.92585	0.3694	0.4291	0
$^5F_1 + ^5G_6$	450	2.0790	9.9929	4.9075	4.9172	0
$^5G_5$	420	2.1003	0.89175	1.0969	0.4619	0

$$\Omega_2 = 1.993 \times 10^{-20}\ cm^2 \qquad \Omega_4 = 2.055 \times 10^{-20}\ cm^2 \qquad \Omega_6 = 1.066 \times 10^{-20}\ cm^2$$
$$\delta_{rms} = 0.5659 \times 10^{-20}\ cm^2$$

Hypersensitive transitions (HSTs) are transitions associated with all absorptions, e.g., Ho^{3+}: $^5I_8 \rightarrow ^5G_5$ transitions. These transitions are very sensitive to the surrounding local environment of the doped ions and follow the selection criteria $\Delta L \leq 2$, $\Delta J \leq 2$, and $\Delta S = 0$ [51–53].

It is well known that parameter Ω_2 represents HSTs and is dependent on the short-range effects of rare-earth ions (the covalency and asymmetry in the community). The ion site is more centro-symmetric and its chemical interaction with the ligand is more ionic when the value of Ω_2 is smaller, both of which contribute to the covalent nature [54]. The massive (bulk) characteristics of the host glass, such as its basicity and strength, are associated with the constants Ω_4 and Ω_6. In addition, the vibrational levels related to the essential rare-earth ions confined to the ligand atoms have a significant impact on them [55–57]. The host glass's basicity and hardness increase with increasing values of Ω_4 and Ω_6. The three Ho^{3+} intensity parameters follow the trend $\Omega_4 > \Omega_2 > \Omega_6$, according to an analysis of the data in Table 5.

The spectroscopic quality factor $(\chi = \Omega_4/\Omega_6)$ is an important characteristic in predicting the luminescence efficiency [58]. In the sample TKWN1, the value calculated is 1.93, which is higher than those of previously reported Ho^{3+}-single-doped samples [59,60].

To predict the emission performance in the studied glass (TKWN1), the radiative properties, such as the radiative transition probabilities $(A_{rad}(J \rightarrow J\prime) = A_{ed} + A_{md})$, branching ratios $(\beta_{rad}(JJ\prime))$, and radiative lifetimes (τ_{rad}), for the $(J \rightarrow J\prime)$ transitions for spontaneous emission are calculated through JO intensity parameters. All data computed are tabulated in Table 6. Compared to fluorophosphate (90.42 s^{-1}) [61], tellurite (165.8 s^{-1}) [60], and germanate glass (69.2 s^{-1}) [62], the TKWN1 sample examined in this study has A_{rad} in

which the $Ho^{3+} \rightarrow {}^5I_7 \rightarrow {}^5I_8$ transition was high and equal to 38.7 s^{-1}. This is determined by the higher refractive index ($n = 1.98$) of the tellurite glass, because the larger refractive index of the host glass, the higher the radiative transition probability, which provides a better likelihood of achieving laser action [63]. Thus, the TKWN1 is possibly a suitable material that might be able to achieve 2 µm fluorescence via the Ho^{3+}: ${}^5I_7 \rightarrow {}^5I_8$ transition.

Table 6. Calculated radiative parameters of different states of Ho^{3+}-single-doped tellurite glass (TKWN1).

Transition	$\bar{\nu}$ (cm^{-1})	n	S_{ed} (pm^2)	S_{md} (pm^2)	A_{ed} (s^{-1})	A_{md} (s^{-1})	β (%)	τ_r (ms)
${}^5I_7 \rightarrow {}^5I_8$	5102	1.9884	1.9505	0.8670	195	43.6554	100.0000	4.1983
${}^5I_6 \rightarrow {}^5I_8$	8658	1.9959	0.8305	0	475	0	86.1550	
${}^5I_6 \rightarrow {}^5I_7$	3556	1.9874	1.3362	1.2450	52	24.4519	13.8450	1.8124
${}^5I_5 \rightarrow {}^5I_8$	11148	2.0040	0.1201	0	177	0	40.9162	
${}^5I_5 \rightarrow {}^5I_7$	6046	1.9897	0.9896	0	225	0	52.0198	2.3152
${}^5I_5 \rightarrow {}^5I_6$	2612	1.9873	1.0679	1.2050	19	11.0797	7.0640	
${}^5I_4 \rightarrow {}^5I_8$	13333	2.0124	0.0082	0	26	0	7.6306	
${}^5I_4 \rightarrow {}^5I_7$	8231	1.9947	0.1720	0	22	0	36.0841	
${}^5I_4 \rightarrow {}^5I_6$	4675	1.9880	1.3163	0	168	0	49.8021	2.9607
${}^5I_4 \rightarrow {}^5I_5$	2185	1.9872	1.2959	0.7640	17	5.0263	6.4831	
${}^5F_5 \rightarrow {}^5I_8$	15504	2.0226	1.5178	0	6272	0	78.3197	
${}^5F_5 \rightarrow {}^5I_7$	10402	2.0014	1.2166	0	1446	0	18.0502	
${}^5F_5 \rightarrow {}^5I_6$	6846	1.9913	0.8152	0	270	0	3.3668	0.1249
${}^5F_5 \rightarrow {}^5I_5$	4356	1.9877	0.2474	0	21	0	0.2610	
${}^5F_5 \rightarrow {}^5I_4$	2171	1.9872	0.0174	0	0	0	0.0023	
${}^5S_2 \rightarrow {}^5I_8$	18882	2.0449	0.2202	0	3808	0	55.6069	
${}^5S_2 \rightarrow {}^5I_7$	13080	2.0114	0.4431	0	2357	0	34.4197	
${}^5S_2 \rightarrow {}^5I_6$	9524	1.9986	0.2033	0	405	0	5.9170	
${}^5S_2 \rightarrow {}^5I_5$	7034	1.9917	0.1105	0	87	0	1.2745	0.1460
${}^5S_2 \rightarrow {}^5I_4$	4848	1.9881	0.7365	0	189	0	2.7603	
${}^5S_2 \rightarrow {}^5F_5$	2678	1.9873	0.0345	0	1	0	0.0217	
${}^5F_4 \rightarrow {}^5I_8$	18868	2.0448	1.2702	0	12173	0	79.3540	
${}^5F_4 \rightarrow {}^5I_7$	13766	2.0143	0.4581	0	1589	0	10.3557	
${}^5F_4 \rightarrow {}^5I_6$	10210	2.0008	0.7410	0	1016	0	6.6243	
${}^5F_4 \rightarrow {}^5I_5$	7720	1.9933	0.7804	0	455	0	2.9631	0.0652
${}^5F_4 \rightarrow {}^5I_4$	5535	1.9889	0.3239	0	69	0	0.4486	
${}^5F_4 \rightarrow {}^5F_5$	3364	1.9873	0.6371	0.3620	30	8.6944	0.2541	
${}^5F_4 \rightarrow {}^5S_2$	686	1.9872	0.0400	0	0	0	0.0001	
${}^5F_3 \rightarrow {}^5I_8$	20619	2.0609	0.3649	0	6088	0	45.0747	
${}^5F_3 \rightarrow {}^5I_7$	15517	2.0226	0.7745	0	5043	0	37.3366	
${}^5F_3 \rightarrow {}^5I_6$	11961	2.0070	0.4212	0	1211	0	8.9682	
${}^5F_3 \rightarrow {}^5I_5$	9470	1.9984	0.4917	0	688	0	5.0934	0.0740
${}^5F_3 \rightarrow {}^5I_4$	7285	1.9923	0.6292	0	395	0	2.9249	
${}^5F_4 \rightarrow {}^5F_5$	5115	1.9884	0.3492	0	75	0	0.5567	
${}^5F_3 \rightarrow {}^5S_2$	2437	1.9872	0.0153	0	0	0	0.0026	
${}^5F_3 \rightarrow {}^5F_4$	1751	1.9872	0.3772	0.5800	3	2.5237	0.0427	

As a key parameter influencing the potential laser performance, the absorption (σ_a) and emission (σ_e) cross-sections need to be calculated. The absorption cross-sections corresponding to the ${}^5I_7 \rightarrow {}^5I_8$ transition of Ho^{3+} are first determined from the measured absorption spectra using the Beer–Lambert equation [64,65], while the emission cross-section for the ${}^5I_7 \rightarrow {}^5I_8$ transition of Ho^{3+} is evaluated from the obtained absorption cross-sections based on McCumber's theory [66]. The calculated absorption and emission cross-sections of Ho^{3+} in the range of 1850–2100 nm are displayed in Figure 11. The absorption and emission maxima are located at 1950 nm and 2045 nm, according to Figure 11.
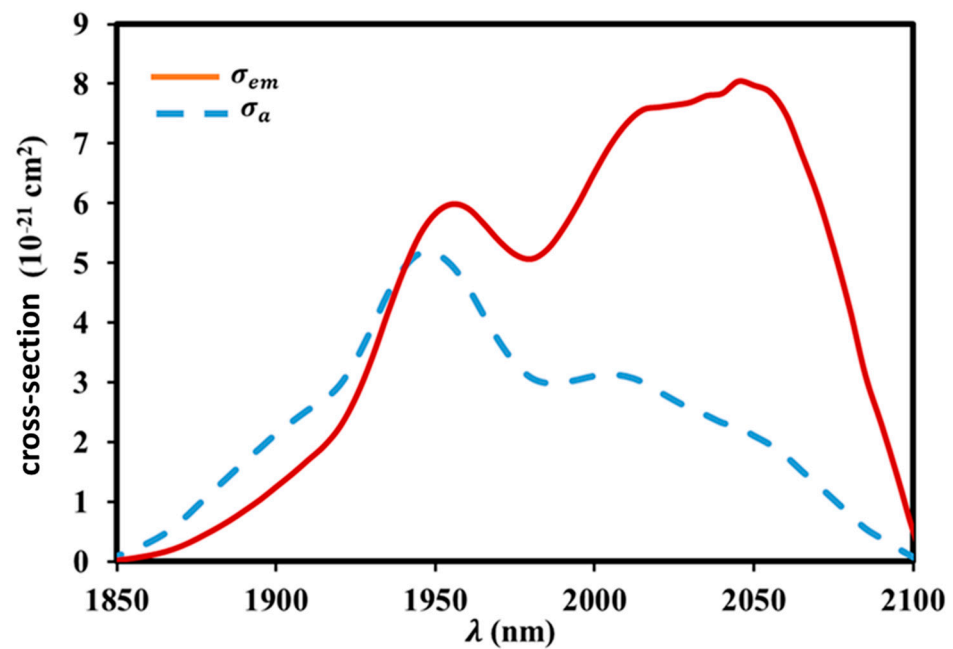
Figure 11. Calculated absorption and emission cross-sections for $^5I_7 \rightarrow {}^5I_8$ transition of Ho^{3+}-ion-doped tellurite glass (TKWN1).

Therefore, the peak value of the stimulated emission cross-section is approximately 8×10^{-21} cm^2. It is smaller than the estimated values for bismuth glass (10.09×10^{-21} cm^2) [67] [68], but it is far larger than that of silicate (3.54×10^{-21} cm^2) [69], fluoride (2.47×10^{-21} cm^2) [70], and germanate glass (3.13×10^{-21} cm^2) [60].

There is a direct correlation between the refractive index of the host glass and the emission cross-section; a higher refractive index increases the possibility of spontaneous radiative transitions. The higher spontaneous radiative transition probability and high refractive index are the primary factors that cause the Ho^{3+} in the produced glass to have an extended emission cross-section.

Additionally, the $FWHM \times \sigma_e$ value is a significant indicator that is often used to define the gain characteristics; the TKWN1 sample corresponds with larger gain properties and a wider gain bandwidth with a higher gain quality value. This study computed that the emission cross-section (σ_e) and $FWHM$ are 8×10^{-21} cm^2 and 150 nm, respectively. Furthermore, as Table 7 illustrates, the $FWHM \times \sigma_e$ is 1200×10^{-28} cm^3 greater than that of a variety of glasses [71]. The TKWN1 sample may have promise as a laser material, according to these findings.

Table 7. Comparison of $FWHM$, σ_e, and $\sigma_e \times FWHM$ values for $^5I_7 \rightarrow {}^5I_8$ transition of TKWN1.

	FWHM (nm)	σ_e (cm^2)	$\sigma_e \times FWHM$ (cm^3)	**Reference**
TKWN1	150	8.0×10^{-21}	1200×10^{-28}	Present work
Silicate	82	5.5×10^{-21}	220×10^{-28}	[71]
Phosphate	78	6.4×10^{-21}	236.8×10^{-28}	[71]
Germanate	84	4.0×10^{-21}	336×10^{-21}	[71]

The wavelength-dependent gain cross-section, which establishes the gain spectrum shape and amplification performance, may be computed using the formula given in a previous article [72] based on the absorption and emission cross-sections of Ho^{3+}. Figure 12 shows the computed gain cross-section spectra of the Ho^{3+}: $^5I_7 \rightarrow {}^5I_8$ radiative transition in the Ho^{3+}-single-doped tellurite glass, with a population inversion value P ranging from 0 to

1 and with an interval of 0.2. It is clear from this spectrum that as the inversion population develops, the gain region moves to longer wavelengths and the gain cross-section improves.
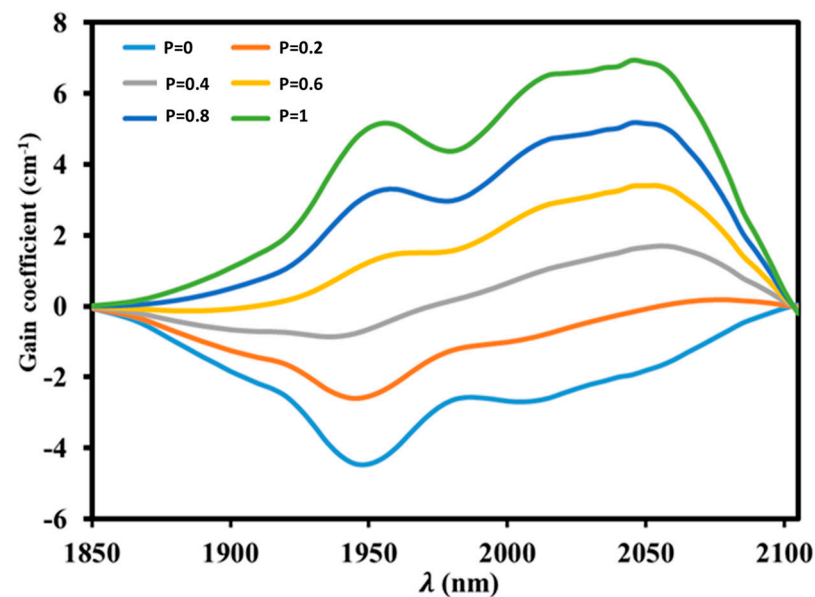

Figure 12. Gain coefficient for $^5I_7 \rightarrow \, ^5I_8$ transition of Ho^{3+}-single-doped tellurite glass (TKWN1).

When compared to germanate glass ($0.47 \, cm^{-1}$), tellurite glass ($1.2 \, cm^{-1}$), and fluorophosphate glass ($0.66 \, cm^{-1}$), the highest gain cross-section at 2045 nm is $6.94 \, cm^{-1}$ [73–75]. A positive gain coefficient indicates a low pump threshold for laser operation when P is 0.6 and λ is greater than 1910 nm [76]. A quasi-three-level system is characterized by an extended positive gain band that increases with P [77].

4. Conclusions

Systematic investigations have been performed to understand the effects of Ho_2O_3, Er_2O_3, and Tm_2O_3 doping on the thermal and optical properties of TeO_2-K_2TeO_3-WO_3-Nb_2O_5 glass. The DSC spectra confirmed the amorphous nature of the as-prepared glasses. Moreover, the DSC spectra showed that the glass transition temperature increased with the incorporation of Er_2O_3 and Tm_2O_3 into the TeO_2-K_2TeO_3-WO_3-Nb_2O_5 glass doped with Ho_2O_3. The thermal stability was investigated through the thermal stability factor ΔT, Hruby's coefficient H, and parameter K_{SP}. The data obtained on the transmittance T and absorbance A for the as-prepared glasses were used to calculate the absorption index α, the refractive index n, the extinction coefficient k, and the optical band gap E_{opt}. The optical band gap E_{opt} and refractive index n slightly increased with the incorporation of Er_2O_3 and Tm_2O_3 into the TeO_2-K_2TeO_3-WO_3-Nb_2O_5 glass doped with Ho_2O_3. Furthermore, the TeO_2-K_2TeO_3-WO_3-Nb_2O_5 glass sample doped with both Ho_2O_3 and Tm_2O_3 displayed the highest values for these parameters. The UV–Vis–NIR absorption and emission spectra of the Ho^{3+}-single-doped, Ho^{3+}/Er^{3+}-co-doped, and Ho^{3+}/Tm^{3+}-co-doped tellurite glasses (TKWN1, TKWN2, and TKWN3, respectively) were examined at room temperature.

The Judd–Ofelt theory was used to determine the full spectroscopic characteristics, radiative lifetimes, branching ratios, and radiative transition probabilities of the TKWN1 sample. Furthermore, McCumber's theory was used to compute the absorption and emission cross-sections of Ho^{3+}: $^5I_7 \rightarrow \, ^5I_8$. There was a maximum emission cross-section of $8 \times 10^{-21} \, cm^2$. Additionally, the gain coefficient of Ho^{3+}, $^5I_7 \rightarrow \, ^5I_8$, the quality factor ($\sigma_e \times FWHM$), and the $FWHM$ were studied. The $FWHM \times \sigma_e$ value was $1200 \times 10^{-28} \, cm^3$, indicating that alternative glasses have greater gain characteristics. Hence, the TKWN1 sample has potential to be utilized as a host material for 2 μm mid-infrared solid-state lasers.

References

1. Jagannath, G.; Eraiah, B.; Gaddam, A.; Fernandes, H.R.; Brazete, D.; Jayanthi, K.; Krishnakanth, K.N.; Rao, S.V.; Ferreira, J.M.F.; Annapurna, K.; et al. Structural and femtosecond third-order nonlinear optical properties of sodium borate oxide glasses: Effect of antimony. *J. Phys. Chem. C* **2019**, *123*, 5591–5602. [CrossRef]

2. Shanmugavelu, B.; Ravi Kanth Kumar, V.; Kuladeep, R.; Rao, D. Narayana, Third order nonlinear optical properties of bismuth zinc borate glasses. *J. Appl. Phys.* **2013**, *114*, 243103. [CrossRef]

3. El-Ghany, H. Physical and optical characterization of manganese ions in sodium–zinc–phosphate glass matrix. *IARJSET* **2018**, *5*, 43–53. [CrossRef]

4. Gandhi, Y.; Mohan, N.K.; Veeraiah, N. Role of nickel ion coordination on spectroscopic and dielectric properties of ZnF_2–As_2O_3–TeO_2: NiO glass system. *J. Non-Cryst. Solids* **2011**, *357*, 1193–1202. [CrossRef]

5. Lakshminarayana, G.; Qiu, J.; Brik, M.G.; Kumar, G.A.; Kityk, I.V. Spectral analysis of Er^{3+}-, Er^{3+}/Yb^{3+}-and $Er^{3+}/Tm^{3+}/Yb^{3+}$-doped TeO_2–ZnO–WO_3–TiO_2–Na_2O glasses. *J. Phys. Condens. Matter* **2008**, *20*, 375101. [CrossRef]

6. Pandey, S.D.; Samanta, K.; Singh, J.; Sharma, N.D.; Bandyopadhyay, A.K. Bandyopadhyay, Raman scattering of rare earth sesquioxide Ho_2O_3: A pressure and temperature dependent study. *J. Appl. Phys.* **2014**, *116*, 133504. [CrossRef]

7. Bashar, K.A.; Lakshminarayana, G.; Baki, S.O.; Mohammed, A.-B.F.A.; Caldino, U.; Meza-Rocha, A.N.; Singh, V.; Kityk, I.V.; Mahdi, M.A. Tunable white-light emission from Pr^{3+}/Dy^{3+} co-doped B_2O_3-TeO_2-PbO-ZnO-Li_2O-Na_2O glasses. *Opt. Mater.* **2019**, *88*, 558–569. [CrossRef]

8. Wantana, N.; Kaewnuam, E.; Damdee, B.; Kaewjaeng, S.; Kothan, S.; Kim, H.; Kaewkhao, J. Energy transfer-based emission analysis of Eu^{3+} doped Gd_2O_3-$CaOSiO_2$-B_2O_3 glasses for laser and X-rays detection material applications. *J. Lumin.* **2018**, *194*, 75–81. [CrossRef]

9. Wang, G.; Xu, S.; Dai, S.; Zhang, J.; Jiang, Z. Thermal stability and spectroscopic properties of Yb^{3+}-doped zinc–tungsten–tellurite glasses. *J. Alloys Compd.* **2004**, *373*, 246–251. [CrossRef]

10. Himei, Y.; Osaka, A.; Namba, T.; Miura, Y. Coordination change of Te atoms in binary tellurite glasses. *J. Non-Cryst. Solids* **1994**, *177*, 164–169. [CrossRef]

11. Kim, S.; Yoko, T. Nonlinear optical properties of TeO_2-based glasses: MO_x–TeO_2 (M = Sc, Ti, V, Nb, Mo, Ta, and W) binary glasses. *J. Am. Ceram. Soc.* **1995**, *78*, 1061–1065. [CrossRef]

12. Gaafar, M.S.; Marzouk, S.Y. Mechanical and structural studies on sodium borosilicate glasses doped with Er_2O_3 using ultrasonic velocity and FTIR spectroscopy. *Phys. B Condens. Matter* **2007**, *388*, 294. [CrossRef]

13. Wang, M.-T.; Cheng, J.-S.; Li, M.; He, F. Structure and properties of soda lime silicate glass doped with rare earth. *Phys. B Condens. Matter* **2011**, *406*, 187–191. [CrossRef]

14. El-Okr, M.; Ibrahem, M.; Farouk, M. Structure and properties of rare-earth-doped glassy systems. *J. Phys. Chem. Solids* **2008**, *69*, 2564–2567. [CrossRef]

15. Al-Syadi, A.M.; Al-Assiri, M.S.; Hassan, H.M.A.; El Enany, G.; El-Desoky, M.M. Effect of sulfur addition on the electrochemical performance of lithium-vanadium-phosphate glasses as electrodes for energy storage devices. *J. Electroanal. Chem.* **2017**, *804*, 36–41. [CrossRef]

16. Hussein, K.I.; Al-Syadi, A.M.; Alqahtani, M.S.; Elkhoshkhany, N.; Algarni, H.; Reben, M.; Yousef, E.S. Thermal Stability, Optical Properties, and Gamma Shielding Properties of Tellurite Glass Modified with Potassium Chloride. *Materials* **2022**, *15*, 2403. [CrossRef]

17. Krishna, G.; Veeraiah, N.; Venkatramaiah, N.; Venkatesan, R. Induced crystallization and physical properties of Li_2O–CaF_2–P_2O_5: TiO_2 glass system: Part, I. Characterization, spectroscopic and elastic properties. *J. Alloys Compd.* **2008**, *450*, 477–485. [CrossRef]

18. Blanchandin, S.; Thomas, P.; Marchet, P.; Champarnaud-Mesjard, J.-C.; Frit, B. Equilibrium and non-equilibrium phase diagram within the TeO_2-rich part of the TeO_2-Nb_2O_5 system. *J. Mater. Chem.* **1999**, *9*, 1785–1788. [CrossRef]

19. Blanchandin, S.; Marchet, P.P.; Thomas, P.; Champarnaud-Mesjard, J.-C.; Frit, B.; Chagraoui, A. New investigations within the TeO_2-WO_3 system: Phase equilibrium diagram and glass crystallization. *J. Mater. Sci.* **1999**, *34*, 4285–4292. [CrossRef]

20. Carreaud, J.; Labruyère, A.; Dardar, H.; Moisy, F.; Duclère, J.-R.; Couderc, V.; Bertrand, A.; Dutreilh-Colas, M.; Delaizir, G.; Hayakawa, T.; et al. Lasing effects in new Nd^{3+}-doped TeO_2–Nb_2O_5–WO_3 bulk glasses. *Opt. Mater.* **2015**, *47*, 99–107. [CrossRef]

21. Reben, M.; Burtan-Gwizdała, B.; Cisowski, J.; Grelowska, I.; Yousef, E.S.; Bukalska, J. Influence of modifiers on thermal and optical properties of TeO_2–P_2O_5–ZnO–PbF_2 glasses. *Opt. Appl.* **2019**, *49*.

22. Bahgat, A.A.; Moustafa, M.G.; Shaisha, E.E. Enhancement of electric conductivity in transparent glass–ceramic nanocomposites of Bi_2O_3–$BaTiO_3$ glasses. *J. Mater. Sci. Technol.* **2013**, *29*, 1166–1176. [CrossRef]

23. Yousef, E.S.; Al-Qaisi, B. Kinetics and fabrication nanocrystallization of optical tellurophosphate glasses in system as: $TeO_2 \cdot P_2O_5 \cdot ZnO \cdot LiNbO_3$. *J. Alloys Compd.* **2012**, *538*, 193–200. [CrossRef]

24. Yousef, E.S. Characterization of oxyfluoride tellurite glasses through thermal, optical and ultrasonic measurements. *J. Phys. D Appl. Phys.* **2005**, *38*, 3970. [CrossRef]

25. Yousef, E.S.; Damak, K.; Maalej, R.; Rüssel, C. Thermal stability and UV–Vis-NIR spectroscopy of a new erbium-doped fluorotellurite glass. *Phil. Mag.* **2012**, *92*, 899. [CrossRef]

26. Yousef, E.S.; Hotzel, M.; Russel, C. Linear and non-linear refractive indices of tellurite glasses in the system TeO_2–WO_3–ZnF_2. *J. Non-Cryst. Solids* **2004**, *342*, 82. [CrossRef]

27. Sestak, J. Applicability of DTA to the Study of Crystallization Kinetics of Glasses. *Phys. Chem. Glas.* **1974**, *15*, 137.

28. Hruby, A. Evaluation of glass-forming tendency by means of DTA. *Czechoslov. J. Phys.* **1972**, *22*, 1187. [CrossRef]

29. Sidkey, M.A.; Gaafar, M.S. Ultrasonic studies on network structure of ternary TeO_2–WO_3–K_2O glass system. *Phys. B Condens. Matter* **2004**, *348*, 46–55. [CrossRef]

30. Lakshminarayana, G.; Kaky, K.M.; Baki, S.O.; Lira, A.; Nayar, P.; Kityk, I.V.; Mahdi, M.A. Physical, structural, thermal, and optical spectroscopy studies of TeO_2–B_2O_3–MoO_3–ZnO–R_2O (R = Li, Na, and K)/MO (M = Mg, Ca, and Pb) glasses. *J. Alloys Compd.* **2017**, *690*, 799–816. [CrossRef]

31. Elkhoshkhany, N.; Mohamed, H.M.; Yousef, E.S. UV–Vis-NIR spectroscopy, structural and thermal properties of novel oxyhalide tellurite glasses with composition TeO_2-B_2O_3-$SrCl_2$-LiF-Bi_2O_3 for optical application. *Results Phys.* **2019**, *13*, 102222. [CrossRef]

32. Oo, H.M.; Mohamed-Kamari, H.; Wan-Yusoff, W.M.D. Optical properties of bismuth tellurite-based glass. *Int. J. Mol. Sci.* **2012**, *13*, 4623–4631. [CrossRef] [PubMed]

33. Yousef, E.S.; Al-Qaisi, B. UV spectroscopy, refractive indices and elastic properties of the $(76 - x) TeO_2 \cdot 9P_2O_5 \cdot 15ZnO \cdot xLiNbO_3$ glass. *Solid State Sci.* **2013**, *19*, 6–11. [CrossRef]

34. Al-Assiri, M.S.; El-Desoky, M.M.; Alyamani, A.; Al-Hajry, A.; Al-Mogeeth, A.; Bahga, A.A. Spectroscopic study of nanocrystalline $V_2O_5 \cdot nH_2O$ films doped with Li ions. *Opt. Laser Technol.* **2010**, *422*, 994–1003. [CrossRef]

35. Ghosh, G. Sellmeier coefficients and dispersion of thermo-optic coefficients for some optical glasses. *Appl. Opt.* **1997**, *36*, 1540–1546. [CrossRef]

36. Ghosh, G. Sellmeier coefficients and chromatic dispersions for some tellurite glasses. *J. Am. Ceram. Soc.* **1995**, *78*, 2828–2830. [CrossRef]

37. Abd-Elnaiem, A.M.; Moustafa, S.; Abdelraheem, A.M.; Abdel-Rahim, M.A.; Mahmoud, A.Z. Effects of annealing on structural and optical properties of Ge20Se70Sn10 thin films for optoelectronic applications. *J. Non-Cryst. Solids* **2020**, *549*, 120353. [CrossRef]

38. Wemple, S.; DiDomenico, M., Jr. Behavior of the electronic dielectric constant in covalent and ionic materials. *Phys. Rev. B* **1971**, *3*, 1338–1351. [CrossRef]

39. Elkhoshkhany, N.; Marzoukb, S.Y.; Moataza, N.; Kandil, S.H. Structural and optical properties of TeO_2-Li_2O-ZnO-Nb_2O_5-Er_2O_3 glass system. *J. Non-Cryst. Solids* **2018**, *500*, 289. [CrossRef]

40. Maaoui, M.; Haouari, Z.; Zaaboub, I.; Fraj, F.; Saidi, H.; Ouada, B. Concentration effects on the optical spectroscopic properties of Er^{3+}-doped TeO_2–Nb_2O_5–ZnO vitreous system. *J. Alloys. Compd.* **2016**, *663*, 395.

41. Taherunnisa, S.; Rudramamba, K.S.; KrishnaReddy, D.V.; Venkateswarlu, T.; Zhydachevskyy, Y.; Suchocki, A.; Piasecki, M.; RamiReddy, M. Efficient 2.01 μm mid-infrared (MIR) and visible emission in Ho^{3+} doped phosphate glasses enhanced by Er^{3+} ions. *Infrared Phys. Techn.* **2020**, *107*, 103294. [CrossRef]

42. Kıbrıslı, O.; Erol, E.; Vahedigharehchopogh, N.; Yousef, E.S.; Ersundu, M.C.; Ersundu, A.E. Noninvasive optical temperature sensing behavior of Ho^{3+} and Ho^{3+}/Er^{3+} doped tellurite glasses through up and down-converted emissions. *Sens. Actuators A* **2020**, *315*, 112321. [CrossRef]

43. Wang, C.; Tian, Y.; Gao, X.; Liu, Q.; Huang, F.; Li, B.; Zhang, J.; Xu, S. Mid-infrared fluorescence properties, structure and energy transfer around 2 μm in Tm^{3+}/Ho^{3+} co-doped tellurite glass. *J. Lumin.* **2017**, *194*, 791–796. [CrossRef]

44. Qi, F.; Huang, F.; Wang, T.; Lei, R.; Zhang, J.; Xu, S.; Zhang, L. Influence of Tm^{3+} ions on the amplification of Ho^{3+}: $^5I_7 \rightarrow {}^5I_8$ transition in fluoride glass modified by $Al(PO_3)_3$ for applications in midinfrared optics. *Chin. Opt. Lett.* **2017**, *15*, 62–67.

45. Ebendorff-Heidepriem, H.; Szabó, I.; Rasztovits, Z.E. Crystallization behavior and spectroscopic properties of Ho^{3+}-doped ZBYA-fluoride glass. *Opt. Mater.* **2000**, *14*, 127–136. [CrossRef]

46. Guan, P.; Fan, X.; Li, W.; Liu, X.; Yu, C.; Zhang, L.; Hu, L. High-efficiency ~2 μm laser in a single-mode Tm-doped lead germanate composite fiber. *Chin. Opt. Lett.* **2016**, *14*, 72–75.

47. Xia, L.; Li, C.; Ding, J.; Li, J.; Zhou, Y.; Zhang, Y. Enhanced 2.7 μm mid-infrared emission in Er^{3+}/Ho^{3+} co-doped tellurite glass. *Opt. Laser Technol.* **2021**, *138*, 106913.

48. Yusof, N.N.; Ghoshal, S.K.; Jupri, S.A. Luminescence of Neodymium Ion-Activated Magnesium Zinc Sulfophosphate Glass: Role of Titanium Nanoparticles Sensitization. *Opt. Mater.* **2020**, *109*, 110390. [CrossRef]

49. Siva Rama Krishna Reddy, K.; Swapna, K.; Mahamuda, S.; Venkateswarlu, M.; Rao, A.S. Structural, optical and photoluminescence properties of alkaline-earth boro tellurite glasses doped with trivalent Neodymium for 1.06 μm optoelectronic devices. *Opt. Mater.* **2021**, *111*, 110615. [CrossRef]

50. Yao, S.; Lv, S.; Feng, Z. Judd-Ofelt analysis of Ho^{3+} doped $CaYAlO_4$ single crystal. *J. Lumin.* **2021**, *238*, 118219. [CrossRef]

51. RekhaRani, P.; Venkateswarlu, M.; Swapna, K.; Mahamuda, S.; Srinivas Prasad, M.V.V.K.; Rao, A.S. Spectroscopic and luminescence properties of Ho^{3+} ions doped barium lead alumino fluoro borate glasses for green laser applications. *Solid State Sci.* **2020**, *102*, 106175.

52. Babu, P.; Seo, H.J.; Kesavulu, C.R.; Jang, K.H.; Jayasankar, C.K. Thermal and Optical Properties of Er^{3+}-Doped Oxyfluorotellurite Glasses. *J. Lumin.* **2009**, *129*, 444. [CrossRef]

53. Cases, R.; Chammaro, M.A. Judd-Ofelt analysis and multiphonon relaxations of rare earth ions in fluorohafnate glasses. *J. Solid State Chem.* **1991**, *90*, 313. [CrossRef]

54. Raja, J.; Amjad Dousti, M.R.; Sahar, M.R. Spectroscopic investigation and Judd–Ofelt analysis of silver nanoparticles embedded Er^{3+}-doped tellurite glass. *Curr. Appl. Phys.* **2015**, *15*, 1–7.

55. Leal, J.J.; Narro-García, R.; Desirena, H.; Marconi, J.D.; Rodríguez, E.; Linganna, K.; De la Rosa, E. Spectroscopic properties of tellurite glasses co-doped with E^{r3+} and Yb^{3+}. *J. Lumin.* **2015**, *162*, 72–80. [CrossRef]

56. Suthanthirakumar, P.; Karthikeyan, P.; Manimozhi, P.K.; Marimuthu, K. Structural and spectroscopic behavior of Er^{3+}/Yb^{3+} co-doped boro-tellurite glasses. *J. Non-Cryst. Solids* **2015**, *10*, 26–34. [CrossRef]

57. Zhao, G.Y.; Tian, Y.; Wang, X.; Fan, H.Y.; Hu, L.L. Spectroscopic properties of 1.8 μm emission in Tm3+ doped bismuth silicate glass. *J. Lumin.* **2013**, *134*, 837–841.

58. Watekar, P.R.; Ju, S.; Han, W.T. Optical properties of Ho-doped alumino–germano-silica glass optical fiber. *J. Non-Cryst. Solids.* **2008**, *354*, 1453–1459. [CrossRef]

59. Xu, X.C.; Zhou, Y.X.; Wang, S.; Wei, S.L.; Dai, S.X.; Wang, X.S. Near-infrared emission and energy transfer mechanism of Tm^{3+}/Yb^{3+} codoped tellurite glasses. *J. Optoelectron. Laser* **2012**, *8*, 1500–1508.

60. Zhang, Q.; Chen, G.; Zhang, G. Spectroscopic properties of Ho^{3+}/Yb^{3+} codoped lanthanum aluminum germanate glasses with efficient energy transfer. *J. Appl. Phys.* **2009**, *106*, 113102–113106. [CrossRef]

61. Tian, Y.; Xu, R.; Zhang, L.; Hu, L.; Zhang, J. Enhanced effect of Ce^{3+} ions on 2 μm emission and energy transfer properties in Yb^{3+}/Ho^{3+} doped fluorophosphate glasses. *J. Appl. Phys.* **2011**, *109*, 083535. [CrossRef]

62. Zhang, Q.; Ding, J.; Shen, Y.; Zhang, G.; Lin, G.; Qiu, J.; Chen, D. Infrared emission properties and energy transfer between Tm^{3+} and Ho^{3+} in lanthanum aluminum germanate glasses. *J. Opt. Soc. Am. B* **2010**, *27*, 975–980. [CrossRef]

63. Heo, J.; Shin, Y.B.; Jang, J.N. Spectroscopic analysis of Tm^{3+} in PbO-Bi_2O_3-Ga_2O_3 glass. *Appl. Opt.* **1995**, *34*, 4284. [CrossRef]

64. Damak, K.; Maâlej, R.; Yousef, E.S.; Qusti, A.H.; Rüssel, C. Thermal and spectroscopic properties of Tm^{3+} doped TZPPN transparent glass laser material. *J. Non-Cryst. Solids* **2012**, *358*, 2974. [CrossRef]

65. Yousef, E.S. Er^{3+} ions doped tellurite glasses with high thermal stability, elasticity, absorption intensity, emission cross section and their optical application. *J. Alloys Compd.* **2013**, *561*, 234. [CrossRef]

66. Payne, S.A.; Chase, L.L.; Smith, L.K.; Kway, W.L. Infrared cross-section measurements for crystals doped with Er^{3+}, Tm^{3+}, and Ho^{3+}. *IEEE J. Quantum Electron.* **1992**, *28*, 2619–2630. [CrossRef]

67. Zhou, D.; Jin, D.; Ni, Q.; Song, X.; Bai, X.; Han, K. Fabrication of double-cladding Ho^{3+}/Tm^{3+} co-doped Bi_2O_3–GeO_2–Ga_2O_3–BaF_2 glass fiber and its performance in a 2.0-μm laser. *J. Am. Ceram. Soc.* **2019**, *102*, 4748–4756. [CrossRef]

68. Li, K.; Wang, G.; Zhang, J.; Hu, L. Broadband 2 μm emission in Tm^{3+}-Ho^{3+} co-doped TeO_2-WO_3-La_2O_3 glass. *Solid State Commun.* **2010**, *150*, 1915–1918. [CrossRef]

69. Li, M.; Liu, X.; Guo, Y.; Hu, L.; Zhang, J. Energy transfer characteristics of silicate glass doped with $Er^{3+,}$ Ho^{3+}, Tm^{3+} for 2 μm emission. *J. Appl. Phys.* **2013**, *114*, 2–9. [CrossRef]

70. Florez, A.; Oliveira, S.L.; Florez, M. Spectroscopic characterization of Ho^{3+} iondoped fluoride glass. *J. Alloys Compd.* **2006**, *418*, 238–242. [CrossRef]

71. Yi, L.X.; Wang, M.; Feng, S.Y.; Chen, Y.K.; Wang, G.H.; Hu, L.L.; Zhang, J.J. Emissions properties of Ho^{3+}: $^5I_7 \rightarrow {}^5I_8$ transition sensitiezed by Er^{3+} and Yb^{3+} in fluorophosphates glasses. *Opt. Mater.* **2009**, *31*, 1586–1590. [CrossRef]

72. McCumber, D.E. Theory of phonon terminated optical masers. *Phys. Rev.* **1964**, *34*, A299–A306. [CrossRef]

73. Fan, J.; Fan, Y.; Yang, Y.; Chen, D.; Calvez, L.; Zhang, X.; Zhang, L. Spectroscopic properties and energy transfer in Yb^{3+}-Ho^{3+} co-doped germanate glass emitting at 2.0 μm. *J. Non-Cryst. Solids* **2011**, *357*, 2431–2434. [CrossRef]

74. Li, K.; Zhang, Q.; Fan, S.; Zhang, L.; Zhang, J.; Hu, L. Mid-infrared luminescence and energy transfer characteristics of Ho^{3+}/Yb^{3+} codoped lanthanum–tungsten–tellurite glasses. *Opt. Mater.* **2010**, *33*, 31–35. [CrossRef]

75. Tian, Y.; Zhang, L.; Feng, S.; Xu, R.; Hu, L.; Zhang, J. 2 μm Emission of Ho^{3+}-doped fluorophosphate glass sensitized by Yb^{3+}. *Opt. Mater.* **2010**, *32*, 1508–1513. [CrossRef]

76. Wang, W.C.; Yuan, J.; Liu, X.Y.; Chen, D.D.; Zhang, Q.Y.; Jiang, Z.H. An efficient 1.8 μm emission in Tm^{3+} and Yb^{3+}/Tm^{3+} doped fluoride modified germinate glasses for a diode-pump mid-infrared laser. *J. Non-Cryst. Solids* **2014**, *404*, 19–25. [CrossRef]

77. Zou, X.; Toratani, H. Spectroscopic properties and energy transfers in Tm^{3+} singly-and Tm^{3+}/Ho^{3+} doubly-doped glasses. *J. Non-Cryst. Solids* **1996**, *195*, 113–124. [CrossRef]